A Direct Model Predictive Control Strategy with an Implicit Modulator for Six-Phase PMSMs

Yitong Wu, *Student Member, IEEE*, Zhen Zhang, *Senior Member, IEEE*, Qifan Yang, *Student Member, IEEE*, Wei Tian, *Member, IEEE*, Petros Karamanakos, *Senior Member, IEEE*, Marcelo Lobo Heldwein, *Senior Member, IEEE*, Ralph Kennel, *Senior Member, IEEE*

***Abstract*—This paper proposes a direct model predictive control (MPC) scheme for asymmetric six-phase permanent magnet synchronous machines (PMSMs), which combines control and modulation in one computation stage. By emulating the switching pattern of space vector modulation (SVM), the MPC problem is formulated as a four-dimensional current control problem where the switching sequences and instants are computed and directly applied to the inverters. This implicit modulation addresses the issue of a variable switching frequency and spread harmonic spectra of conventional direct MPC methods. Moreover, the effect of the modulation constraints and controller bandwidth on the system performance is investigated as well. To verify the effectiveness of the proposed control strategy, experiments are carried out with an asymmetric six-phase PMSM driven by two three-phase two-level inverters.**

***Index Terms*—Model predictive control, implicit modulator, multi-phase machines, harmonic elimination, modulation constraints.**

I. Introduction

In recent decades, multi-phase machines have obtained significant attention due to their potential application in drive systems. Compared to traditional three-phase machines, the multi-phase structure features power splitting, lower torque ripple, and better fault tolerance [1]–[4]. Thanks to the advantages above, multi-phase machines are considered to be suitable for high-power applications such as electric vehicles and railway traction, electric ships and aircraft propulsion, and wind power generation systems [5]–[7]. In particular, multi-three-phase machines are preferred for their compatibility with standard three-phase power converters, where the asymmetric six-phase machine is the simplest configuration [8]. To achieve a completely decoupled machine model, vector space decomposition (VSD) in an asymmetric six-phase system projects the original six-dimensional space into three orthogonal subspaces defined as $\alpha\beta$, xy, and o_1o_2 [9]. The current in the $\alpha\beta$ subspace contributes to the electromagnetic torque generation, while the xy component gives rise to harmonic distortions and increases the copper losses. Hence the xy current elimination is a critical issue for the efficiency improvement in multi-phase drive systems. Recently, model predictive control (MPC) applied to multi-phase electric drives has been a relevant research topic thanks to its numerous advantages. MPC features excellent transient performance and flexible design that can account for multiple control objectives and explicit constraints [10]–[12]. However, the conventional direct MPC methods display high current distortion and torque ripples, which result from the fact that the single optimal voltage in the finite control set cannot exactly track the voltage reference and minimize the xy current [13]. Accordingly, the design of an implicit modulator to improve the steady-state performance is a critical issue for direct MPC. Aiming to eliminate the harmonic distortion, both the modulation and control problems take into account the xy components by using additional voltage vectors and current loops [14]. The use of virtual voltage vectors (VVs) integrated in MPC schemes can effectively reduce the xy current, where two active voltage vectors are pre-synthesized to obtain the null xy voltage [15]. Moreover, [15] adopted a virtual voltage vector with a zero voltage vector during one interval, achieving lower torque ripples and a fixed switching frequency at low speeds. However, a null xy voltage generated by the open-loop control cannot fully minimize the xy current due to the impedance imbalance, which causes the current imbalance between the two sets of windings. In [16], the effect of the xy current is formulated as a closed-loop direct MPC problem to compensate for the imbalanced current, and a pair of virtual vectors and a zero vector are adopted to enhance the tracking of the $\alpha\beta$ current references. To address the issues above, this paper proposes a direct MPC algorithm with an implicit modulator that emulates the behavior of space vector modulation (SVM) suitable for an asymmetric six-phase permanent magnet synchronous motor (PMSM) fed by two three-phase two-level voltage source inverters (2L-VSI). The proposed control strategy manages to minimize the torque ripple and the xy current, and consequently the copper losses. To do so, the four-dimensional state model is first established on the d, q, x, and y-axes. Then, considering the active durations of each voltage vector in one sampling interval as the only optimization variable, the proposed direct MPC algorithm is formulated as a quadratic program (QP) which is

Manuscript received December 31st, 2021; revised March 16th and April 17th, 2022; accepted April 19th, 2022. This work was supported in part by the National Natural Science Foundation of China under Project 51977138, in part by the Humboldt Research Fellowship under Ref. 3.5-CHN-1201512-HFST-P, and in part by the Deutsche Forschungsgemeinschaft (DFG, German Research Foundation) under Project 432509817 and 418870390. (*Corresponding author: Wei Tian*)

Y. Wu, and Z. Zhang, are with the School of Electrical and Information Engineering, Tianjin University, Tianjin 300072, China; e-mail: wuyitong@tju.edu.cn, zhangz@tju.edu.cn

Q. Yang, W. Tian, M. Heldwein and R. Kennel, are with the Chair of High-Power Converter Systems, Technical University of Munich, 80333 Munich, Germany; e-mail: qifan.yang@tum.de, wei.tian@tum.de, marcelo.heldwein@tum.de, ralph.kennel@tum.de

P. Karamanakos is with the Faculty of Information Technology and Communication Sciences, Tampere University, 33101 Tampere, Finland; e-mail: p.karamanakos@ieee.org

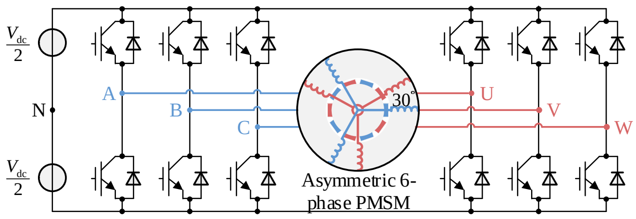

Fig. 1: Scheme of asymmetric six-phase PMSM drive.

easy to solve in real time. Moreover, a disturbance observer is designed to compensate for the parameter mismatches of the machine. Finally, the effectiveness of the algorithm is experimentally verified, and its (steady-state and dynamic) performance is compared with those of field oriented control (FOC) with carrier based-pulse width modulation (CB-PWM) and a conventional continuous-control-set MPC (CCS-MPC). The remainder of this article is organized as follows. The mathematical model of the used asymmetric six-phase PMSM and the voltage vectors of the inverters are briefly introduced in Section II. The design of the disturbance observer, SVM method, and direct MPC problem are presented in Section III. The subsection focused on the SVM method includes the guidelines for selecting candidate vectors, the assessment of modulation constraints and the pattern analysis. The utilized dual-sector solution for improved optimality and the whole process of the direct MPC algorithm is provided in the same section. Moreover, the experimental results are presented in Section IV to validate efficacy of the proposed direct MPC algorithm. Finally, conclusions are drawn in Section V.

II. Mathematical Model Of The System

A. Model of Asymmetric 6-ph PMSMs

Fig. 1 depicts the drive system under study, which consists of a six-phase asymmetrical PMSM with two isolated neutral points powered by two three-phase 2L-VSIs. Due to the complex inductance model of the two coupling windings, the VSD model is widely used to analyze the effects on system performance of voltage, current, and flux in each phase. According to the VSD theory, the six-demensional space is decomposed into three orthogonal subspaces, namely the $\alpha\beta$, xy, and o_1o_2 subspaces, while different harmonics are mapped to different subspaces. Among the three subspaces, the fundamental and harmonic components in the $\alpha\beta$ subspace contribute to the energy conversion. On the other hand, harmonics in the xy subspace increase the stator copper losses, while the o_1o_2 components are zero due to the symmetrical machine and the two floating star points of the load. Hence, the o_1o_2 subspace is omitted in the following modeling derivation. Accordingly, the $\alpha\beta$ subspace is transformed into the synchronous dq frame, but the xy remains in the stationary frame. Considering the model uncertainties, the model of the six-phase PMSM under the dq and xy frames is described as

$$\frac{\mathrm{d}}{\mathrm{d}t}\boldsymbol{i} = \boldsymbol{F}\boldsymbol{i} + \boldsymbol{G}\boldsymbol{v} + \boldsymbol{w} + \boldsymbol{d}, \tag{1}$$

where $\boldsymbol{i}$, $\boldsymbol{v}$, $\boldsymbol{w}$, and $\boldsymbol{d} \in \mathbb{R}^{4\times 1}$ are the vectors of stator current, voltage, back-electromotive force (EMF), and current disturbances, respectively. The vectors above are formulated as

$$\boldsymbol{i} = \begin{bmatrix} i_\mathrm{d} & i_\mathrm{q} & i_\mathrm{x} & i_\mathrm{y} \end{bmatrix}^\mathrm{T}, \tag{2a}$$

$$\boldsymbol{v} = \begin{bmatrix} v_\mathrm{d} & v_\mathrm{q} & v_\mathrm{x} & v_\mathrm{y} \end{bmatrix}^\mathrm{T}, \tag{2b}$$

$$\boldsymbol{w} = \begin{bmatrix} 0 & -\frac{\omega_\mathrm{e}\psi_\mathrm{PM}}{L_\mathrm{q}} & 0 & 0 \end{bmatrix}^\mathrm{T}, \tag{2c}$$

where ω_e is the rotor electrical angular speed and ψ_PM is the amplitude of the fundamental component of the permanent magnet flux. It is important to highlight that $\boldsymbol{d}$ from parameter mismatches and other unmeasurable disturbances can be estimated with a disturbance observer, presented in Section III. The state matrix $\boldsymbol{F}$ and input matrix $\boldsymbol{G}$ in (1) are given by

$$\boldsymbol{F} = \begin{bmatrix} -\frac{R_\mathrm{s}}{L_\mathrm{dq}} & \omega_\mathrm{e} & 0 & 0 \\ -\omega_\mathrm{e} & -\frac{R_\mathrm{s}}{L_\mathrm{dq}} & 0 & 0 \\ 0 & 0 & -\frac{R_\mathrm{s}}{L_\mathrm{xy}} & 0 \\ 0 & 0 & 0 & -\frac{R_\mathrm{s}}{L_\mathrm{xy}} \end{bmatrix}, \tag{3a}$$

$$\boldsymbol{G} = \mathrm{diag}\left\{\frac{1}{L_\mathrm{dq}}, \frac{1}{L_\mathrm{dq}}, \frac{1}{L_\mathrm{xy}}, \frac{1}{L_\mathrm{xy}}\right\}, \tag{3b}$$

where R_s is the stator resistance, L_d, L_q and L_xy are the inductances of two sets of windings on d-axis, q-axis, and xy subspaces, respectively [16], [17]. Note that according to (3b), the magnetic coupling between the dq- and xy-subsystems and cross-saturation are neglected. This simplification, however, does not adversely affect the system performance as shown in Section IV. Nevertheless, for operation where, e.g., saturation of the magnetic material of the machine is prominent, the full inductance model should be considered to account for all differential inductances, see, e.g., [18], [19]. Based on (1) and (3), the discrete-time state-space model is deduced as

$$\boldsymbol{i}(k+1) = \boldsymbol{A}\boldsymbol{i}(k) + \boldsymbol{B}\boldsymbol{v}(k) + \boldsymbol{z} + \boldsymbol{e}(k), \tag{4a}$$

$$\boldsymbol{y}(k+1) = \boldsymbol{x}(k+1), \tag{4b}$$

where the matrices are calculated via forward Euler of the form $\boldsymbol{A} = \boldsymbol{I} - \boldsymbol{F}T_\mathrm{s}$, $\boldsymbol{B} = \boldsymbol{G}T_\mathrm{s}$, $\boldsymbol{z} = \boldsymbol{w}T_\mathrm{s}$, and $\boldsymbol{e} = \int_t^{t+T_\mathrm{s}} \boldsymbol{d}(\delta)\mathrm{d}\delta$. T_s denotes the sampling interval.

B. Voltage Vectors

As the machine is powered by two three-phase 2L-VSIs, there exists a total of $2^6 = 64$ different switching possibilities whose corresponding voltage components in the $\alpha\beta$ and xy subspaces are displayed in Fig. 2. It should be mentioned that only 48 distinct active voltage vectors and a zero voltage vector are mapped due to redundancy of the switching states. All the vectors are divided into four groups according to their amplitudes in the $\alpha\beta$ subspace, namely large, medium, basic, and small vectors. Due to the largest amplitude in the $\alpha\beta$ subspace and the smallest in xy, large vectors utilize the dc-link voltage to the greatest degree, while causing slight disturbance in harmonics [17], [20]. Accordingly, the proposed MPC method will take advantage of this feature and build its switching strategy by utilizing these large vectors.

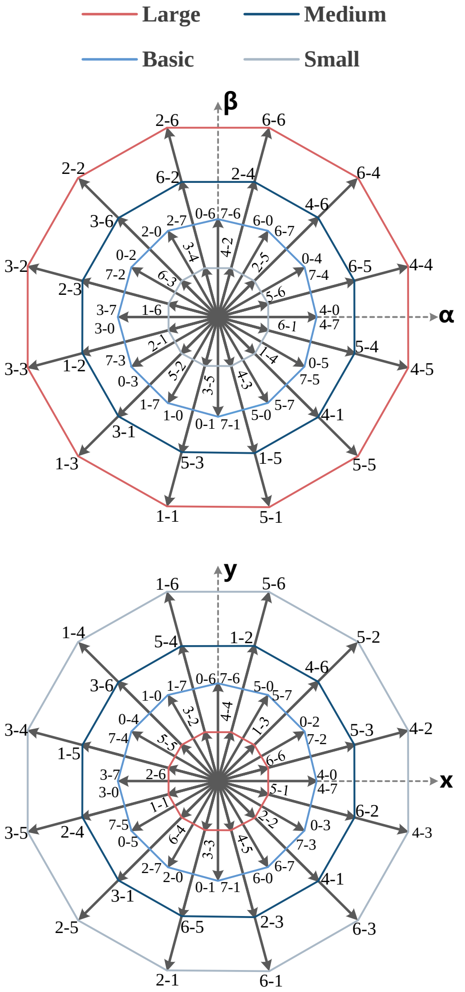

Fig. 2: Voltage vectors of dual-three-phase inverters.

III. Direct Model Predictive Control Strategy with Implicit Modulator

The proposed direct MPC implements the close-loop control of current components in both the $\alpha\beta$ and xy subspaces. Since the performance is strongly dependent on the drive model, it is important to employ a disturbance observer for model correction to avoid potential instability. Besides, the selection of switching sequences and corresponding modulation constraints in direct MPC are discussed in this section. Finally, the objective function and control algorithm are introduced, along with the implementation of the proposed implicit modulator.

A. Design of Disturbance Observer based on Kalman Filter

The main uncertainties of the model are due to the defective knowledge of machine parameters and the presence of unmeasured external disturbances, which causes a continuous error in the current prediction. Consequently, the corresponding trajectory of states may deviate from the references with the bias errors [21], which must be eliminated in the close-loop control for a better tracking performance. As aforementioned, the bias error of current is denoted as $\boldsymbol{e}$, which is assumed

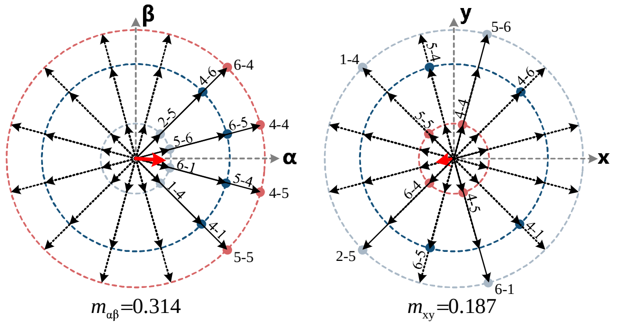

Fig. 3: Demanded (average) stator voltage at low speed/modulation index.

constant during one interval. Hence, the augmented state space including disturbances can be defined as

$$\hat{\boldsymbol{x}}(k+1) = \hat{\boldsymbol{A}}\hat{\boldsymbol{x}}(k) + \hat{\boldsymbol{B}}\boldsymbol{v}(k) + \hat{\boldsymbol{z}}, \tag{5a}$$

$$\hat{\boldsymbol{y}}(k) = \hat{\boldsymbol{C}}\hat{\boldsymbol{x}}(k), \tag{5b}$$

$$\hat{\boldsymbol{A}} = \begin{bmatrix} \boldsymbol{A} & \boldsymbol{I} \\ \boldsymbol{0} & \boldsymbol{I} \end{bmatrix}, \hat{\boldsymbol{B}} = \begin{bmatrix} \boldsymbol{B} \\ \boldsymbol{0} \end{bmatrix}, \hat{\boldsymbol{C}} = \begin{bmatrix} \boldsymbol{I} & \boldsymbol{0} \\ \boldsymbol{0} & \boldsymbol{I} \end{bmatrix}, \hat{\boldsymbol{z}} = \begin{bmatrix} \boldsymbol{z} \\ \boldsymbol{0} \end{bmatrix}, \hat{\boldsymbol{x}} = \begin{bmatrix} \boldsymbol{i} \\ \boldsymbol{e} \end{bmatrix}.$$

The disturbance estimation consists of the following five steps [22].

i) *Prediction of state*:

$$\hat{\boldsymbol{x}}_{\mathrm{p}}(k) = \hat{\boldsymbol{A}}\hat{\boldsymbol{x}}(k-1) + \hat{\boldsymbol{B}}\boldsymbol{v}(k-1) + \hat{\boldsymbol{z}} \tag{6a}$$

$$\hat{\boldsymbol{y}}_{\mathrm{p}}(k) = \hat{\boldsymbol{C}}\hat{\boldsymbol{x}}_{\mathrm{p}}(k). \tag{6b}$$

ii) *Estimation of the error covariance matrix*:

$$\boldsymbol{P}_{\mathrm{p}} = \hat{\boldsymbol{A}}\boldsymbol{P}\hat{\boldsymbol{A}}^{\mathrm{T}} + \boldsymbol{Q}, \tag{7}$$

where $\boldsymbol{Q}$ is the covariance of the process noise.

iii) *Computation of the Kalman filter gain*:

$$\boldsymbol{K} = \boldsymbol{P}_{\mathrm{p}}\hat{\boldsymbol{C}}^{\mathrm{T}}\left[\hat{\boldsymbol{C}}\boldsymbol{P}_{\mathrm{p}}\hat{\boldsymbol{C}}^{\mathrm{T}} + \boldsymbol{R}\right]^{-1}, \tag{8}$$

where $\boldsymbol{R}$ is the covariance of the observation noise.

iv) *State estimation*:

$$\hat{\boldsymbol{x}}(k) = \hat{\boldsymbol{x}}_{\mathrm{p}}(k) + \boldsymbol{K}(\hat{\boldsymbol{y}}(k) - \hat{\boldsymbol{y}}_{\mathrm{p}}(k)). \tag{9}$$

v) *Update of the error covariance matrix*:

$$\boldsymbol{P}(k+1) = \left(\boldsymbol{I} - \boldsymbol{K}\hat{\boldsymbol{C}}\right)\boldsymbol{P}_{\mathrm{p}}. \tag{10}$$

B. Four-Large-Vector Modulation

For the xy current reduction, the conventional four-vectors-SVM (4V-SVM) is widely employed, where four active vectors (most are large vectors) are applied simultaneously to ensure $\boldsymbol{v}_{\mathrm{xy}} = \boldsymbol{0}$ [20], [23]. This open-loop control strategy of xy components is dependent on the ideal industrial situation which contains no impedance imbalance between the two three-phase windings. In practice, the method based on $\boldsymbol{v}^*_{\mathrm{xy}} = \boldsymbol{0}$ partly reduces copper losses, however, it cannot fully compensate for potential current imbalances between the two three-phase windings due to inevitable asymmetries [24], [25]. Therefore, the principle of four-vector SVM is adopted and refined to achieve favorable close-loop control of the xy components.

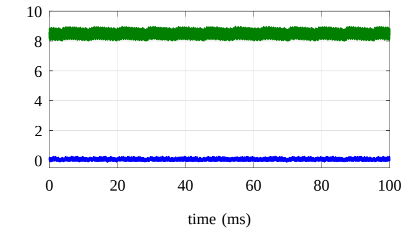

(a) Stator current in dq-plane (A).

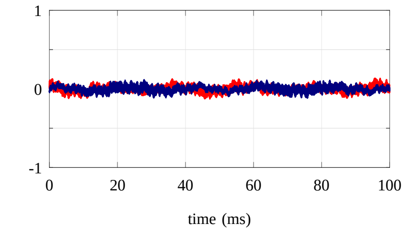

(b) Stator current in xy-plane (A).

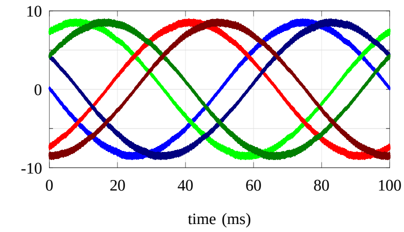

(c) Six-phase currents (A).

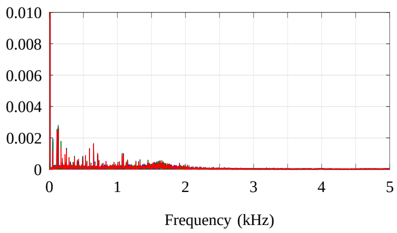

(d) Normalized stator current spectrum, THD = 2.50 %.

Fig. 4: The machine current using large vectors.

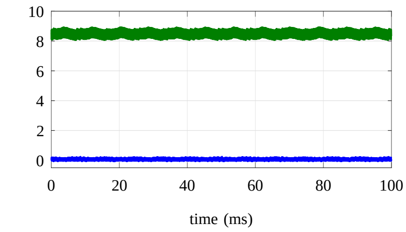

(a) Stator current in dq-plane (A).

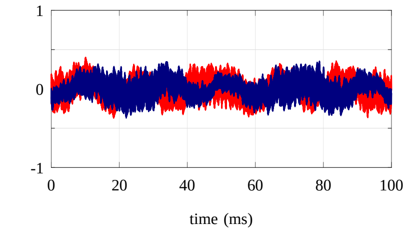

(b) Stator current in xy-plane (A).

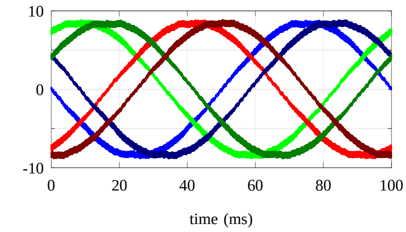

(c) Six-phase currents (A).

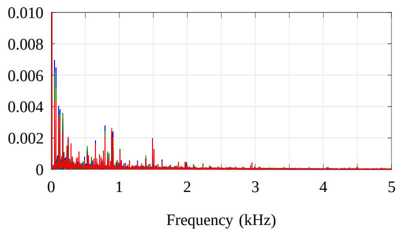

(d) Normalized stator current spectrum, THD = 2.85 %.

Fig. 5: The machine current using medium vectors.

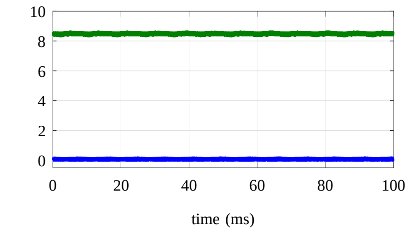

(a) Stator currents in dq-plane (A).

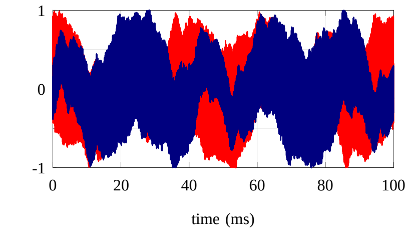

(b) Stator currents in xy-plane (A).

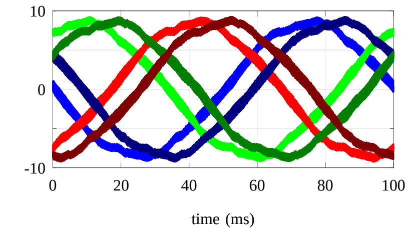

(c) Six-phase currents (A).

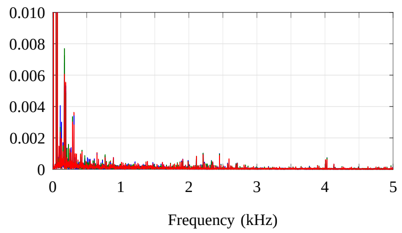

(d) Normalized stator current spectrum, THD = 5.56 %.

Fig. 6: The machine current using small vectors.

1) Voltage Vectors Selection: As aforementioned in Section II, 48 active voltage vectors in four different groups are available in modulation. However, one challenge is how to select candidate vectors to conduct the modulation within each PWM interval. The utilization of the so-called large vectors set can be found in many previous publications on the control of six-phase PMSM. However, the reason of using the large voltage vectors under the whole speed operation is hardly well explained. Accordingly, a detailed discussion on the decision of the used voltage vectors is carried out.

It is straightforward that the large voltage vectors should be used when the demanded voltage of the motor is high. However, as will be shown in the following example, the large voltage vectors are also preferred when the voltage demand of the motor is low. Take Fig. 3 as an example, where we let the motor operate at 20% of its nominal speed. Thus, the demanded voltage of the motor, depicted as the red arrow in Fig. 3, is very low. Under such operation point, using the large vectors (i.e., 6-4, 4-4, 4-5 and 5-5 in Fig. 3) to synthesize the demanded voltage results in higher ripples in the $\alpha\beta$-subspace, comparing with that of using medium vectors (i.e., 4-6, 6-5, 5-4 and 4-1) or small vectors (i.e., 2-5, 5-6, 6-1 and 1-4). However, the medium and small vectors produce larger ripples in the xy-plane, since they have larger amplitude in the xy-plane than the large vectors. The corresponding simulation results are shown in Figs. 4 to 6, which verify the aforementioned analysis. Moreover, using medium or small vector sets also results in more switching actions, as shown in Fig. 7.

2) Unconstrained 4L-SVM: Since the dual three-phase drive system can be regarded as a four-dimensional system, the four nearest vectors out of the outermost 12 vectors in the $\alpha\beta$ subspace will be selected along with the zero vectors, ergo the name 4-large-SVM (4L-SVM). Considering the significance of $\boldsymbol{i}_{\alpha\beta}$ in torque generation, the candidate vectors have to guarantee a wide modulation region in the $\alpha\beta$ subspace. Fig. 8(a) illustrates the vector selection approach. The modulation region in the $\alpha\beta$ subspace is evenly divided into twelve sectors of 30 electric degrees, where the four nearest large vectors that have four corresponding components

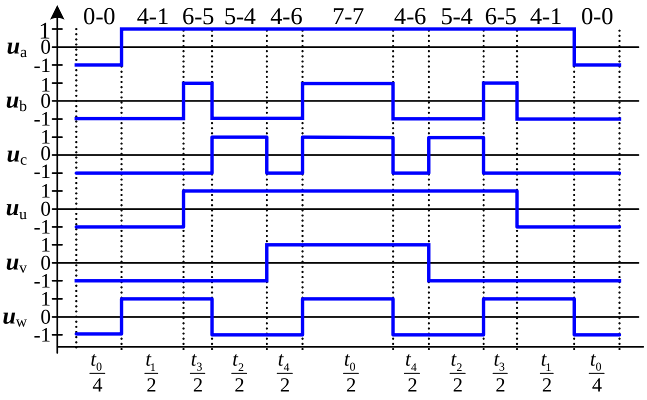

(a) Medium vector set.

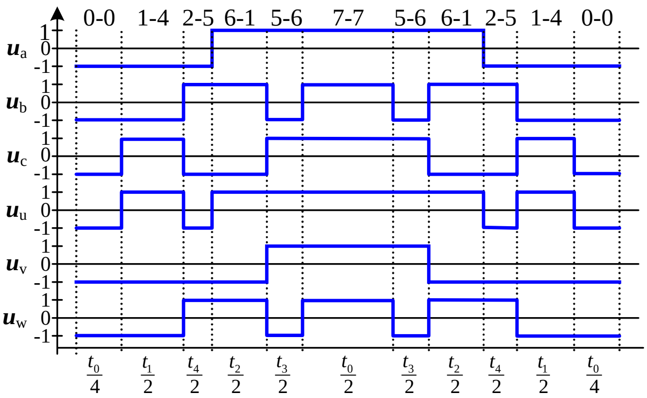

(b) Small vector set.

Fig. 7: Six-phase switch positions.

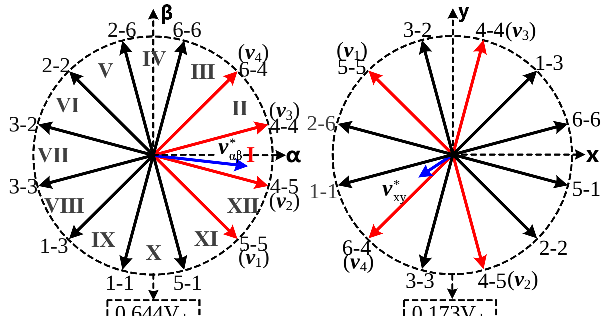

(a)

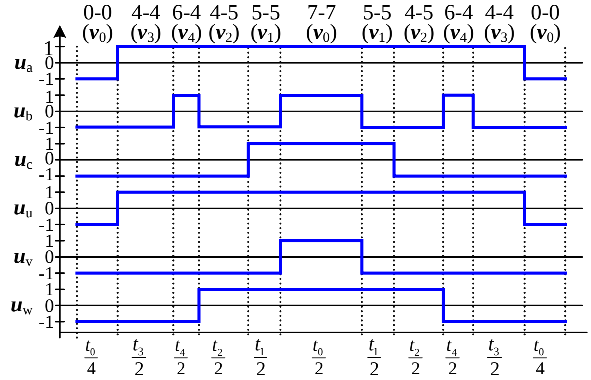

(b)

Fig. 8: 4L-SVM: (a) Sectors and candidate vectors; (b) Pattern of six-phase switch positions in sector I.

in the xy subspace are used in each sector. According to the voltage reference $\boldsymbol{v}^* = [v^*_\alpha; v^*_\beta; v^*_x; v^*_y]$, the sector in which the $\boldsymbol{v}^*_{\alpha\beta}$ is located is selected. For example, assuming $\boldsymbol{v}^*_{\alpha\beta}$ (blue arrow) is inside sector I, the candidate vectors (red arrows) are $\boldsymbol{v}_{5-5}$, $\boldsymbol{v}_{4-5}$, $\boldsymbol{v}_{4-4}$, and $\boldsymbol{v}_{6-4}$. In the counter-clockwise direction, the components in the $\alpha\beta$ and duration of the four candidate vectors are denoted as $\boldsymbol{v}_1$ and t_1, $\boldsymbol{v}_2$ and t_2, $\boldsymbol{v}_3$ and t_3, $\boldsymbol{v}_4$ and t_4, respectively. Then, to achieve reference tracking, a set of linear equation is formulated as

$$\begin{cases} \sum_{i=1}^{4} v^i_\alpha t_i = v^*_\alpha T_s \\ \sum_{i=1}^{4} v^i_\beta t_i = v^*_\beta T_s \\ \sum_{i=1}^{4} v^i_x t_i = v^*_x T_s \\ \sum_{i=1}^{4} v^i_y t_i = v^*_y T_s \end{cases} \tag{11a}$$

$$\text{subject to} \begin{cases} t_i \geq 0 \quad (i = 0, 1, 2, 3, 4) \\ \sum_{i=0}^{4} t_i = T_s \end{cases}. \tag{11b}$$

The solution of this set of equations yields the duration vector $\boldsymbol{t} = [t_1; t_2; t_3; t_4; t_0]$, where t_0 is the duration of the zero vector and i is the identifier of the active and zero vectors.

3) Constraints of 4L-SVM: Due to lack of modulation constraints in (11a), the calculated switching positions and durations cannot be physically implemented under an extremely high modulation index $m_{\alpha\beta} = \frac{|\boldsymbol{v}_{\alpha\beta}|}{V_{dc}/2}$ or $m_{xy} = \frac{|\boldsymbol{v}_{xy}|}{V_{dc}/2}$. Accordingly, (11b) is added to introduce modulation constraints, such that the application times of all voltage vectors are positive and their sum cannot exceed T_s. Different from the conventional SVM, the voltage references $\boldsymbol{v}^*_{\alpha\beta}$ and $\boldsymbol{v}^*_{xy}$ are both non-null. Since the modulation of $\boldsymbol{v}^*_{\alpha\beta}$ and $\boldsymbol{v}^*_{xy}$ are coupled, the constraints analysis is necessary. Specifically, $\boldsymbol{v}^*_{\alpha\beta}$ rotates counterclockwise with a constant angular speed, as defined by the fundamental frequency. On the other hand, the rotational direction of $\boldsymbol{v}^*_{xy}$ is irregular, as this is dictated by the composition of high-order harmonics. Accordingly, the modulation region in the xy subspace must allow all the possible voltage references $\boldsymbol{v}^*_{xy}$ to ensure the optimal control of the drive.

To further discuss the strategy, it should be pointed out that the solution (11a) cannot be applied to the whole modulation region in the sector. Given that the modulation region in the xy subspace is decided by the modulation index in the $\alpha\beta$ subspace, it is essential to investigate whether the constraints are active in such a narrow modulation region [26]. To verify the effectiveness of (11b), a simulation where the deadbeat (DB) control is utilized is carried out to explore whether voltage $\boldsymbol{v}_{xy}$ can track their reference $\boldsymbol{v}^*_{xy}$. As shown in Fig. 9, the results indicate that $\boldsymbol{v}_{xy}$ is located within an extremely small circle where it is easily tracked under the steady-state (with a small modulation index m). However, as the modulation index m exceeds a certain value when a transient occurs, it is impossible for $\boldsymbol{v}_{xy}$ to exactly track $\boldsymbol{v}^*_{xy}$, and thus $\boldsymbol{i}_{xy}$ is uncontrolled. Notably, this does not mean that $\boldsymbol{v}_{xy}$ is too small to be considered as zero, which is similar to the mentioned virtual vectors. It can be seen that under $m = 0.4977$, although the amplitude of $\boldsymbol{v}^*_{xy}$ is

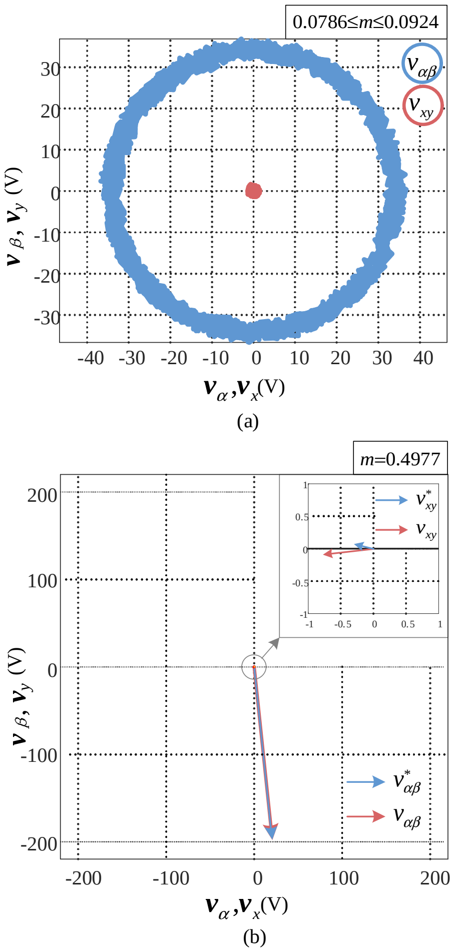

Fig. 9: Modulation constraints in direct MPC with implicit modulator: (a) steady state; (b) transient state.

below 0.5 V, $\boldsymbol{v}_{\mathrm{xy}}$ is generated with an amplitude of 0.8 V. Undoubtedly, these uncontrolled active voltage components in the xy subspace lead to intensive ripples of $\boldsymbol{i}_{\mathrm{xy}}$ which can potentially cause instability. Therefore, a detailed investigation on how to implement a wider xy modulation region is relevant for the dynamic performance, though it is beyond the scope of this work.

4) Pattern analysis: Once the candidate vectors and duration are obtained, the switching sequence $\boldsymbol{U}$ and switching instants $\boldsymbol{t}$ are designed to generate the gate signals. The classic pattern of 4L-SVM adopts the vectors $\boldsymbol{v}_{0-0}$ and $\boldsymbol{v}_{7-7}$ as zero vectors, where the former is located on the sides of the interval and the latter at the center. The four active vectors are inserted between $\boldsymbol{v}_{0-0}$ and $\boldsymbol{v}_{7-7}$ such that the switching frequency is minimized. In doing so, however, the PWM pattern displays an asymmetric seven-segment switching sequence which amplifies the influence of xy harmonics. To avoid this, the implicit modulation strategy proposed in this paper generates a (11-segment) symmetrical switching pattern with respect to the midpoint of the modulation cycle, as shown in Fig. 8(b). This switching strategy, however, comes at a cost of a somewhat increased switching frequency which can be calculated by:

$$f_{\mathrm{sw}} = \frac{4}{3} f_{\mathrm{s}}, \tag{12}$$

where f_{sw} is the switching frequency and f_{s} is the sampling frequency.

C. Direct Model Predictive Current Control

As shown in Fig. 10, the proposed direct MPC consists of two main steps, i.e., the sector selection, and the formulation and solution of the optimization problem to provide the (constrained) application times of the voltage vectors. These steps are described in the sequel of this section.

1) Dual-sectors solution: Firstly, it is necessary to select the candidate vectors to construct the switching sequences during one sampling interval. To this aim, the DB control solution is employed. Specifically, the DB solution that achieves zero current tracking error at the next step $k+1$ is given by

$$\boldsymbol{v}_{\mathrm{unc}}(k) = \boldsymbol{B}^{-1}\left[\boldsymbol{i}^*(k+1) - \boldsymbol{A}\boldsymbol{i}(k) - \boldsymbol{z} - \boldsymbol{e}(k)\right]. \tag{13}$$

Hence the ideal voltage reference $\boldsymbol{v}_{\mathrm{unc}}$ is calculated without considering the modulation constraints. Nevertheless, it is possible that the calculated DB solution violates the constraints when the current reference changes significantly, particularly in the xy subspace. In fact, considering the constraints, the optimal voltage reference $\boldsymbol{v}_{\mathrm{opt}}$ is possibly located in a different sector from the solution of (13). Hence, to avoid excluding the optimal voltage vectors that are required to synthesize the DB solution, the neighboring sectors of the sector the DB solution lies within are also considered. In doing so, optimality is secured. According to the above, as a simplified approach, the dual-sector solution can be adopted that merely considers two adjacent sectors during one interval. As described in the top left of Fig. 11, bounded by the angular bisector, the selected sector N is divided into the forward semi-sector (pink area) and backward semi-sector (blue area) depending on the rotation of the voltage vector (back-EMF). If $\boldsymbol{v}_{\mathrm{unc}}$ is located in the forward semi-sector, sector $N_1 = N$ and $N_2 = N-1$ are selected. For example, if $N = 1$, then sectors I and XII are chosen. Correspondingly, sector $N_1 = N$ and $N_2 = N+1$, i.e., sector I and II, are considered when $\boldsymbol{v}_{\mathrm{opt}}$ is within the backward semi-sector. Fig. 11 also lists the corresponding vectors of the choices between two semi-sectors in sector I. Another interesting finding is that in the dual-sector solution, the modulation constraints in the xy subspace of both sectors (pink area in the top right) are involved in MPC as a union. Thus, the modulation region in the xy subspace is extended under the steady state. Therefore the dual-sector solution does not only effectively crop the search space without influence on the performance, but also extends the feasible region of the optimal control.

2) Objective function: Given that the manipulated variable in 4L-SVM is the duration of switch positions, an additional transformation matrix $\boldsymbol{T}_{\mathrm{svm}}$, given by (14), is necessary to calculate the application times $\boldsymbol{t}(k)$ of the voltage vectors in the selected sector N. The modified predictive model is written as

$$\boldsymbol{i}(k+1) = \boldsymbol{A}\boldsymbol{i}(k) + \boldsymbol{B}\boldsymbol{T}_{\mathrm{park}}\boldsymbol{T}_{\mathrm{svm}}\boldsymbol{t}(k) + \boldsymbol{z} + \boldsymbol{e}(k), \tag{15}$$

where $\boldsymbol{T}_{\mathrm{park}}$ is the matrix of the extended Park transformation.

$$
\boldsymbol{T}_{\mathrm{svm}} = V_{\mathrm{dc}} \begin{bmatrix} 0.644\cos[\frac{(N-1)\pi}{6} - \frac{\pi}{4}] & 0.644\cos[\frac{(N-1)\pi}{6} - \frac{\pi}{12}] & 0.644\cos[\frac{(N-1)\pi}{6} + \frac{\pi}{12}] & 0.644\cos[\frac{(N-1)\pi}{6} + \frac{\pi}{4}] \\ 0.644\sin[\frac{(N-1)\pi}{6} - \frac{\pi}{4}] & 0.644\sin[\frac{(N-1)\pi}{6} - \frac{\pi}{12}] & 0.644\sin[\frac{(N-1)\pi}{6} + \frac{\pi}{12}] & 0.644\sin[\frac{(N-1)\pi}{6} + \frac{\pi}{4}] \\ 0.147\cos[\frac{5(N-1)\pi}{6} + \frac{3\pi}{4}] & 0.147\cos[\frac{5(N-1)\pi}{6} - \frac{5\pi}{12}] & 0.147\cos[\frac{5(N-1)\pi}{6} + \frac{5\pi}{12}] & 0.147\cos[\frac{5(N-1)\pi}{6} - \frac{3\pi}{4}] \\ 0.147\sin[\frac{5(N-1)\pi}{6} + \frac{3\pi}{4}] & 0.147\sin[\frac{5(N-1)\pi}{6} - \frac{5\pi}{12}] & 0.147\sin[\frac{5(N-1)\pi}{6} + \frac{5\pi}{12}] & 0.147\sin[\frac{5(N-1)\pi}{6} - \frac{3\pi}{4}] \end{bmatrix} \tag{14}
$$

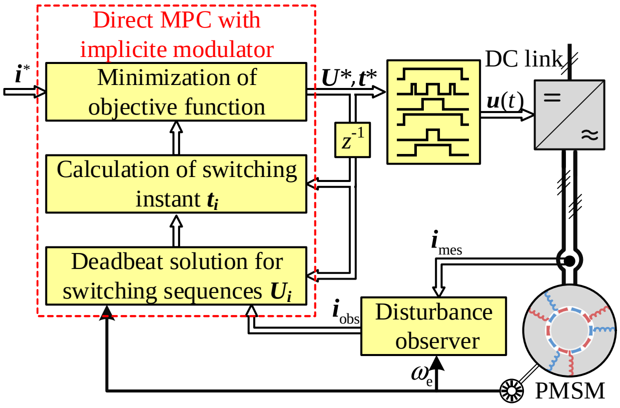

Fig. 10: Direct model predictive current control with implicit modulator for an asymmetric six-phase PMSM supplied by dual three-phase 2L-VSIs.

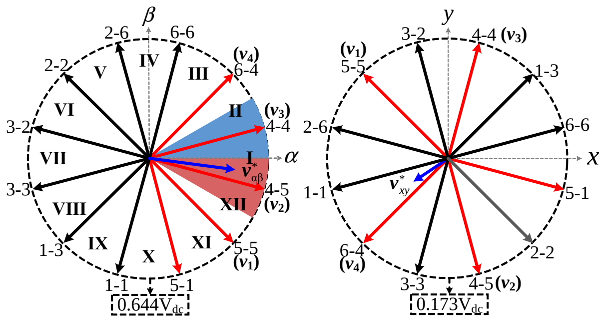

$v^*_{\alpha\beta}$	Sector	Vectors			
Backward semi-sector	I	$v_{5\text{-}5}$	$v_{4\text{-}5}$	$v_{4\text{-}4}$	$v_{6\text{-}4}$
	II	$v_{4\text{-}5}$	$v_{4\text{-}4}$	$v_{6\text{-}4}$	$v_{6\text{-}6}$
Forward semi-sector	I	$v_{5\text{-}5}$	$v_{4\text{-}5}$	$v_{4\text{-}4}$	$v_{6\text{-}4}$
	XII	$v_{5\text{-}1}$	$v_{5\text{-}5}$	$v_{4\text{-}5}$	$v_{4\text{-}4}$

Fig. 11: An example of the dual-sectors solution: sector I.

Given the new prediction model (15), the objective function which accounts for the stator current tracking error is defined as

$$
J = ||\boldsymbol{i}(k+1) - \boldsymbol{i}^*(k+1)||^2_{\boldsymbol{\Lambda}}, \tag{16}
$$

where $\boldsymbol{\Lambda}$ is a weighting matrix for the dq and xy components. Considering the formulation of $\boldsymbol{i}(k+1)$, function (16) can be described as

$$
J = ||\underbrace{\boldsymbol{A}\boldsymbol{i}(k) + \boldsymbol{z} + \boldsymbol{e}(k) - \boldsymbol{i}^*(k+1)}_{\boldsymbol{r}} + \underbrace{\boldsymbol{B}\boldsymbol{T}_{\mathrm{park}}\boldsymbol{T}_{\mathrm{svm}}}_{\boldsymbol{M}}\,\boldsymbol{t}(k)||^2_{\boldsymbol{\Lambda}}. \tag{17}
$$

Algorithm 1 Direct MPC with implicit modulator

Given $\boldsymbol{i}^*(k+1)$, $\boldsymbol{i}(k)$ and $\boldsymbol{e}(k)$
1: Utilize the DB solution to acquire $\boldsymbol{v}_{\mathrm{unc}}(k+1)$
2: Select the candidate switching sequences $\boldsymbol{U}_i$, $i \in \{1,2\}$
3: For each sector: Solve the QP (18).
This yields $\boldsymbol{t}_i$ and J_i.
4: Solve the secondary optimization problem (19).
This yields $\boldsymbol{t}^*$ and $\boldsymbol{u}^*$.
Return $\boldsymbol{t}^*$ and $\boldsymbol{u}^*$.

---

3) Control algorithm: The pseudocode of the control method is summarized in Algorithm 1. In a pre-processing stage, the measured current $\boldsymbol{i}(k)$, estimated disturbance $\boldsymbol{e}(k)$, and the current reference $\boldsymbol{i}^*(k+1)$ are computed. Then the unconstrained reference $\boldsymbol{v}_{\mathrm{unc}}$ is calculated from the DB solution, as the candidate switching sequences $\boldsymbol{U}_1$ and $\boldsymbol{U}_2$ are selected. In the third step, for either switching sequence $\boldsymbol{U}_i$ $(i = 1, 2)$, an optimization problem is formulated to find the duration $\boldsymbol{t}$. With (17), the optimization problem can be stated as

$$
\begin{aligned}
\underset{\boldsymbol{t} \in \mathbb{R}^5}{\text{minimize}} \quad & ||\boldsymbol{r}(k) + \boldsymbol{M}\boldsymbol{t}(k)||^2_{\boldsymbol{\Lambda}} \\
\text{subject to} \quad & t_i \geq 0 \;\; (i = 0, 1, 2, 3, 4) \\
& \sum_{i=0}^{4} t_i = T_{\mathrm{s}},
\end{aligned} \tag{18}
$$

which can be solved efficiently by the method proposed in [27]. The problem (18) is solved twice, once for $\boldsymbol{U}_1$ and the other for $\boldsymbol{U}_2$. Each problem yields the corresponding durations $\boldsymbol{t_1}$ and $\boldsymbol{t_2}$, respectively. The last step selects these combinations of duration and vectors with the minimal value of the objective function

$$
\text{minimize} \quad J_i, \quad i \in \{1,2\}. \tag{19}
$$

The optimal switching sequences and corresponding switching instants are designed as described in Section III-B. Finally, by means of a high-frequency counter, a field programmable gate array (FPGA) applies the switch positions at the appropriate switching instants to the inverters.

IV. Experiment

The proposed direct MPC scheme is implemented on an asymmetric six-phase PMSM supplied by two 2L-VSIs to examine the steady-state and transient-state performance. The experimental setup is shown in Fig. 12. The real-time control platform is a dSPACE SCALEXIO system composed of a 4 GHz Intel XEON processor and a Xilinx Kintex-7 FPGA. Two three-phase two-level SEW MDX inverters are used to

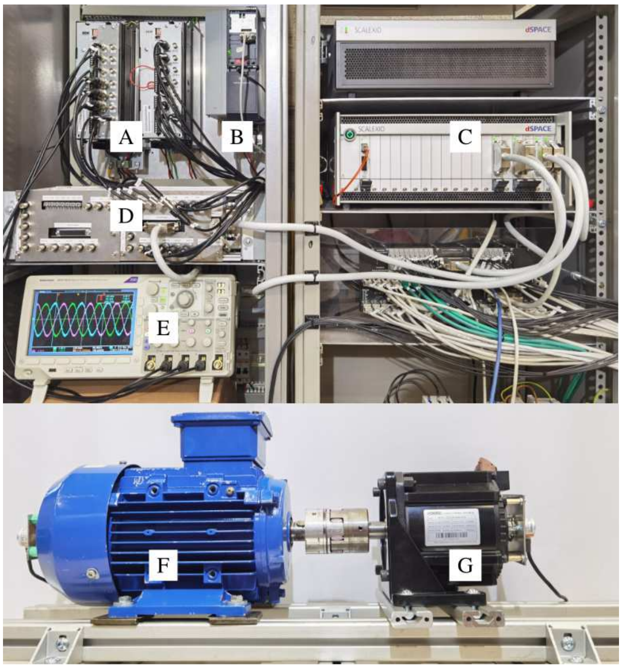

Fig. 12: Setup of the electrical drives testbench. A:two SEW inverters for dual three-phase PMSM; B:Danfoss inverter for load induction machine (IM); C:dSPACE SCALEXIO real-time control system; D:Interface; E:Oscilloscope; F:IM; G:dual-three-phase PMSM.

TABLE I: PARAMETERS OF PMSM

Parameter	Symbol	Value
Rated voltage	U_{N}	220 V
Rated current	I_{N}	6 A
Rated speed	ω_{mN}	2000 1/min
Rated torque	T_{N}	10 N. m
Number of pole pairs	n_{p}	5
Nominal permanent flux	Ψ_{m}	0.18 Wb
Nominal phase resistance	R_{s}	0.45 Ω
Nominal phase inductance	L_{s}	3.5 mH

control the PMSM and a Danfoss inverter is for the load induction machine (IM), all of which are powered by a stiff dc source with a dc-link voltage of 300 V. The switching frequency of the inverter is always kept as $f_{\mathrm{sw}} = 10\,\mathrm{kHz}$. The parameters of the PMSM are given in Table I.

A. Steady-State Performance

Figs. 13 shows the steady-state performance of the drive controlled by the proposed direct MPC scheme while the machine is operating at a fundamental frequency $f_0 = 50\,\mathrm{Hz}$ and at half of the nominal torque. The six-phase current, current components in dq and xy frames, current harmonic spectrum, and the used average voltage of each phase at every sampling interval are presented. As can be observed, i_{d} and i_{q} accurately track their reference. i_{x} and i_{y} are controlled within an amplitude of 0.2 A, hence the phase currents are effectively sinusoidal with a fundamental frequency f_0=50 Hz. As can be seen, the graphs of i_{x} and i_{y} display an inconsistent (non-sinusoidal) oscillation whose frequency is approximately between the 5^{th} and the 7^{th} multiple of f_0. These harmonics can also be observed in the corresponding current spectrum, see Fig. 13(b). For comparison purposes, a linear controller (i.e., FOC) with CB-PWM and common mode injection is carried out. The parameters of the proportional and integral (PI) controllers are adjusted according to the modulus optimal method. The results under steady state displayed in Fig. 14 are similar to those of the direct MPC scheme. The current total harmonic distortion (THD) in FOC is slightly worse than that of direct MPC, though it achieves better $\boldsymbol{i}_{\mathrm{xy}}$ control. This is consistent with the observation of the phase current where FOC produces larger distortion at its peaks. A conventional continuous-control-set MPC (CCS-MPC) method is also implemented for further comparison purposes. More specifically, the objective function is chosen as $J = \|\boldsymbol{i}(k+1) - \boldsymbol{i}^*(k+1)\|^2_{\boldsymbol{\Lambda}}$, where $\boldsymbol{\Lambda} = \mathrm{diag}\{1, 1, \lambda_{\mathrm{xy}}, \lambda_{\mathrm{xy}}\}$ and λ_{xy} is the weighting factor of the $\boldsymbol{i}_{\mathrm{xy}}$. Therefore, the QP problem of the CCS-MPC is formulated as following:

$$\begin{aligned} \underset{\boldsymbol{v}\in\mathbb{R}^4}{\text{minimize}} \quad & \|\boldsymbol{i}(k+1) - \boldsymbol{i}^*(k+1)\|^2_{\boldsymbol{\Lambda}} \\ \text{subject to} \quad & \boldsymbol{i}(k+1) = \boldsymbol{A}\boldsymbol{i}(k) + \boldsymbol{B}\boldsymbol{v}(k) + \boldsymbol{z} + \boldsymbol{e}(k) \\ & \sqrt{v_{\mathrm{d}}^2 + v_{\mathrm{q}}^2} \leq \frac{V_{\mathrm{dc}}}{\sqrt{3}}. \end{aligned} \tag{20}$$

As shown in Fig. 15, the CCS-MPC achieves a very similar steady-state behavior as the proposed direct MPC scheme. The magnitude of the 5^{th} and 7^{th} harmonics are also increased compared to FOC. As can be observed from Figs. 13(d) and 15(d), these harmonics come mainly from the xy-plane. This is because we have used weighting factors λ_{xy} to give higher tracking priority on $\boldsymbol{i}_{\mathrm{dq}}$ and lower priority on $\boldsymbol{i}_{\mathrm{xy}}$, since $\boldsymbol{i}_{\mathrm{dq}}$ directly relates to the electrical-to-mechanical energy conversion. By doing so, the reference tracking of $\boldsymbol{i}_{\mathrm{xy}}$ is compromised. However, the overall THD of the proposed DMPC is slightly lower than that of FOC.

B. Transient Performance

Figs. 16 to 18 and Figs. 19 to 21 compare the performance of the three schemes during a torque step-down and step-up transient, respectively. As can be observed, the proposed direct MPC achieves the fastest referencing tracking in both cases. The transient behavior of FOC is the slowest since the control bandwidth of the PI controllers is significantly lower than that of MPC. Besides, the transient behavior of the proposed direct MPC also outperforms the conventional CCS-MPC with PWM. This is because the proposed direct MPC is a direct control scheme, thus it simultaneously selects the optimal switching vector sets and calculates the optimal switching time. By doing so, the switching position is directly controlled, meaning that the proposed direct MPC strategy can achieve a faster transient than modulator-based MPC schemes, especially when overmodulation is considered. It is worth mentioning that MPC schemes suffer from larger ripples in $\boldsymbol{i}_{\mathrm{xy}}$ during the torque reference step changes. This is because MPC tries to achieve as fast a transient in the dq frame as possible. The exact tracking to $\boldsymbol{i}^*_{\mathrm{dq}}$ is prioritized due to its significant contribution to torque generation, and MPC follows this rule. On the other hand, FOC equally considers $\boldsymbol{i}^*_{\mathrm{dq}}$ and $\boldsymbol{i}^*_{\mathrm{xy}}$, thus resulting in a slower response in the dq frame. Moreover, $\boldsymbol{i}_{\mathrm{xy}}$

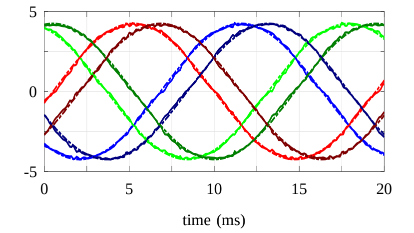

(a) Six-phase currents (A).

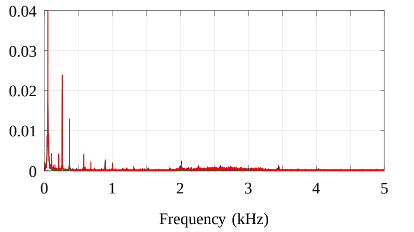

(b) Normalized stator current spectrum, THD = 4.02 %.

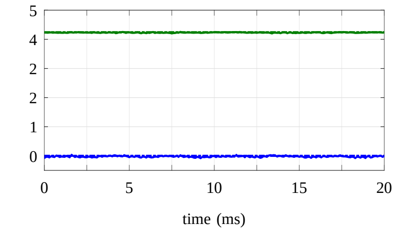

(c) Stator current in dq-plane (A).

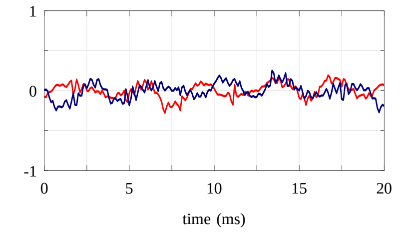

(d) Stator current in xy-plane (A).

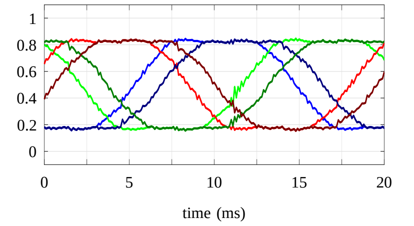

(e) Six-phase used average voltage (p.u.).

Fig. 13: Steady-state behavior of the proposed DMPC.

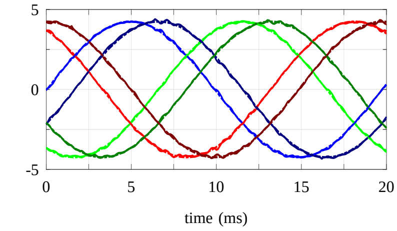

(a) Six-phase currents (A).

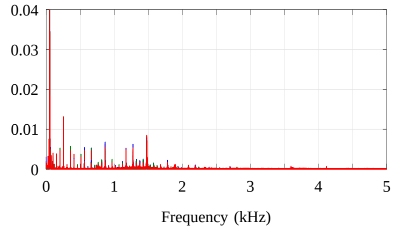

(b) Normalized stator current spectrum, THD = 4.11 %.

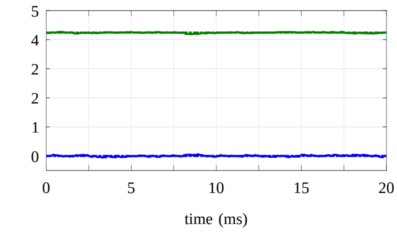

(c) Stator current in dq-plane (A).

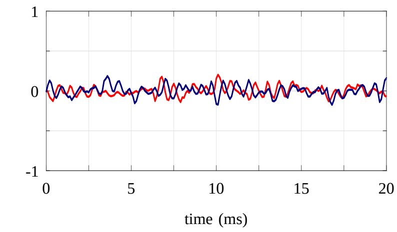

(d) Stator current in xy-plane (A).

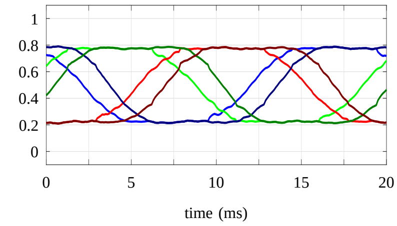

(e) Six-phase used average voltage (p.u.).

Fig. 14: Steady-state behavior of FOC.

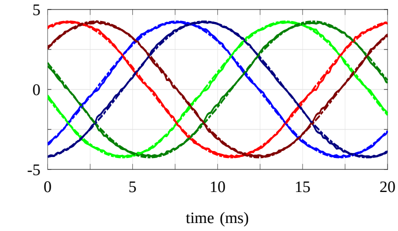

(a) Six-phase currents (A).

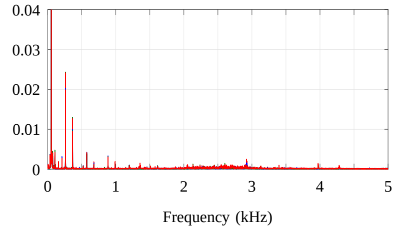

(b) Normalized stator current spectrum, THD = 4.23 %.

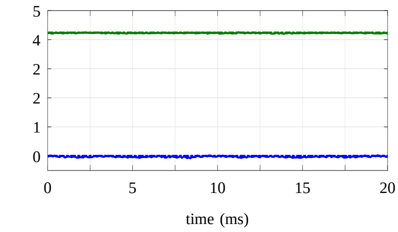

(c) Stator current in dq-plane (A).

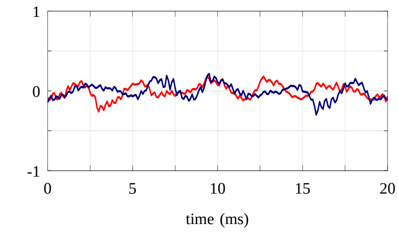

(d) Stator current in xy-plane (A).

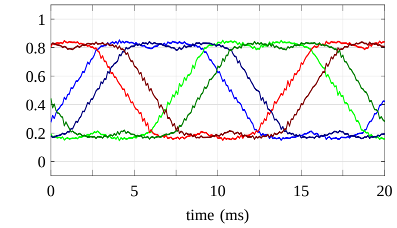

(e) Six-phase used average voltage (p.u.).

Fig. 15: Steady-state behavior of CCS-MPC.

is composed of harmonics which do not participate in torque generation. They only lead to increased harmonic distortions and thus copper losses. Hence, the control of $\boldsymbol{i}_{\mathrm{xy}}$ is more significant at steady state rather at transient. As shown in Figs. 16(b) and 19(b), although MPC schemes suffer from a large, but transient, ripple in $\boldsymbol{i}_{\mathrm{xy}}$ when there is a step-up change in the reference i_{q}^{*}, the effects of these ripples on the six-phase currents are very small. Considering such a short period of time, this ripple essentially does not affect the copper losses. And as mentioned above, this ripple in the xy-plane does not affect the electromagnetic torque.

C. Computational Burden

To evaluate the computational burden of the aforementioned three control schemes, the maximum and average turnaround times in dSPACE are summarized in Table II. As shown, the proposed DMPC needs the longest time since it solves two QPs within each sampling interval. But thanks to the efficient QP solver, the max turnaround time is kept considerably low, i.e., 41.5 µs, which makes the real-time implementation of the proposed DMPC feasible.

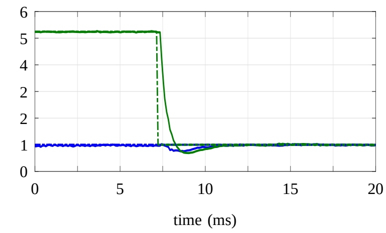

(a) Stator current in dq-plane (A).

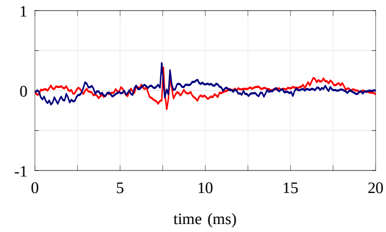

(b) Stator current in xy-plane (A).

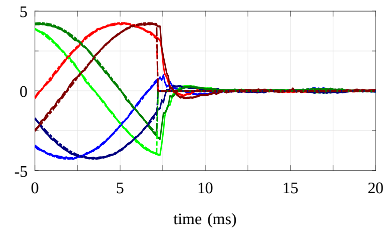

(c) Six-phase currents (A).

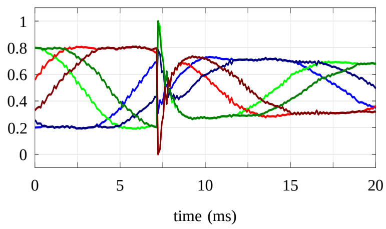

(d) Six-phase used average voltage (p.u.).

Fig. 16: Transient behavior of the proposed DMPC at a torque reference step down.

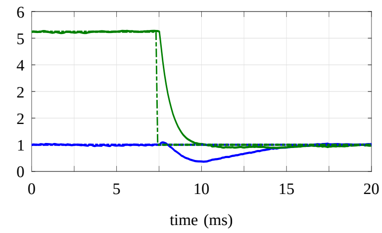

(a) Stator current in dq-plane (A).

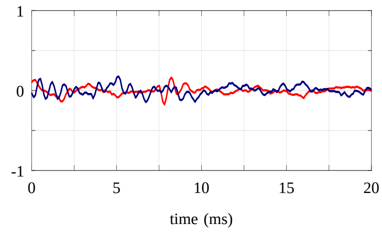

(b) Stator current in xy-plane (A).

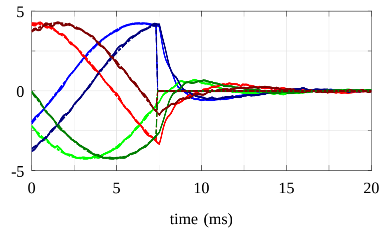

(c) Six-phase currents (A).

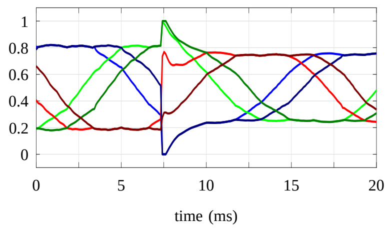

(d) Six-phase used average voltage (p.u.).

Fig. 17: Transient behavior of FOC at a torque reference step down.

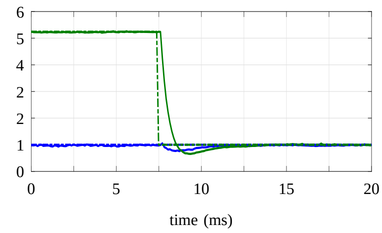

(a) Stator current in dq-plane (A).

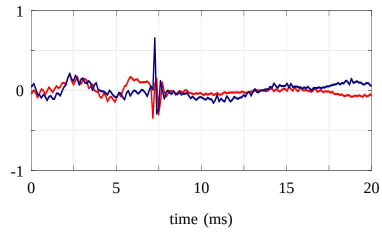

(b) Stator current in xy-plane (A).

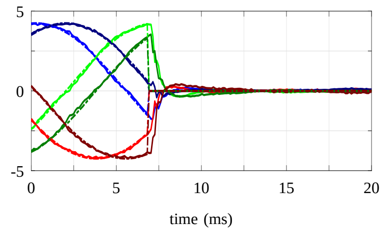

(c) Six-phase currents (A).

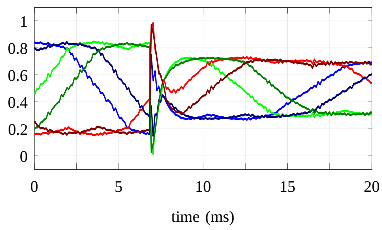

(d) Six-phase used average voltage (p.u.).

Fig. 18: Transient behavior of CCS-MPC at a torque reference step down.

TABLE II: The maximum and average turnaround time of the three discussed control algorithms running on dSPACE.

	DMPC	FOC	CCS-MPC
Max Turnaround time (µs)	41.5	11.2	30.7
Average turnaround time (µs)	35.7	10.7	23.7

V. Conclusion

This paper proposed an direct MPC scheme with an implicit modulator that minimizes the stator current error and copper losses. To avoid potential performance degradation due to parameter mismatches, model uncertainties, etc., a disturbance observer based on a Kalman filter is implemented. Moreover, an optimization problem is formulated that accounts for the large voltage vectors, according to the 4L-SVM principle, such that current reference tracking on the dq and xy subplanes is simultaneously achieved. To ensure optimality, a dual sector selection process is adopted which yields the optimal switching sequences and corresponding switching instants at which a new switch position needs to be applied. Subsequently, the optimal voltage vectors are applied at the corresponding switching instants by emulating an SVM pattern. Finally, to keep the computational complexity modest, instead of considering all the possible sectors and corresponding switching sequences in the optimization process, the DB solution is utilized to limit the set of candidate solutions. The presented results demonstrated the effectiveness of the proposed method. Specifically, direct MPC achieves better steady-state performance with lower harmonic distortions (and thus copper losses) as compared with conventional FOC and CCS-MPC. Moreover, the dynamic behavior of the proposed method is superior thanks to its direct control principle.

References

[1] E. Levi, "Advances in converter control and innovative exploitation of additional degrees of freedom for multiphase machines," *IEEE Trans. Ind. Electron.*, vol. 63, no. 1, pp. 433–448, Jan. 2016.

[2] J. Karttunen, S. Kallio, P. Peltoniemi, P. Silventoinen, and O. Pyrhönen, "Dual three-phase permanent magnet synchronous machine supplied by two independent voltage source inverters," in *International Symposium on Power Electronics Power Electronics, Electrical Drives, Automation and Motion*, Sorrento, Italy, Jun. 2012, pp. 741–747.

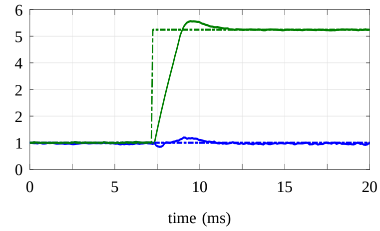

(a) Stator current in dq-plane (A).

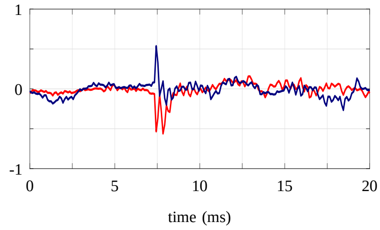

(b) Stator current in xy-plane (A).

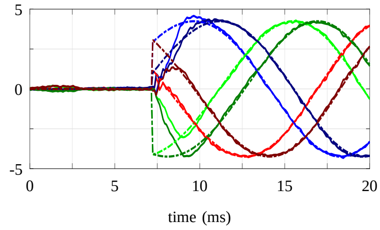

(c) Six-phase currents (A).

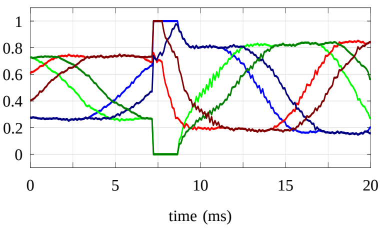

(d) Six-phase used average voltage (p.u.).

Fig. 19: Transient behavior of the proposed DMPC at a torque reference step up.

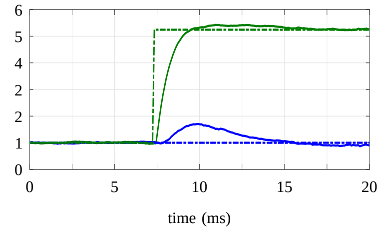

(a) Stator current in dq-plane (A).

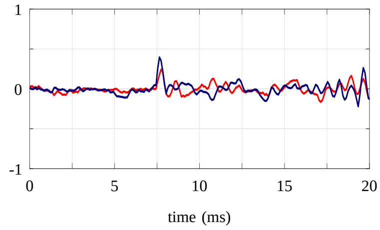

(b) Stator current in xy-plane (A).

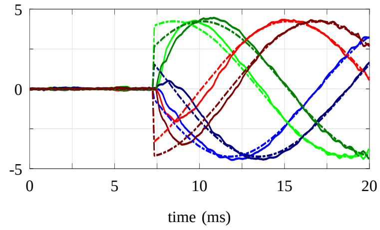

(c) Six-phase currents (A).

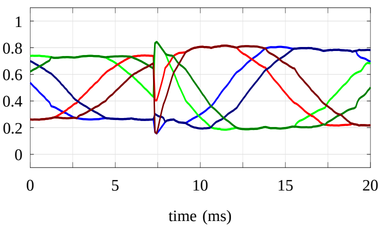

(d) Six-phase used average voltage (p.u.).

Fig. 20: Transient behavior of FOC at a torque reference step up.

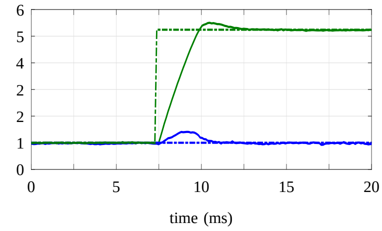

(a) Stator current in dq-plane (A).

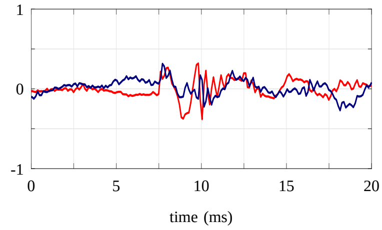

(b) Stator current in xy-plane (A).

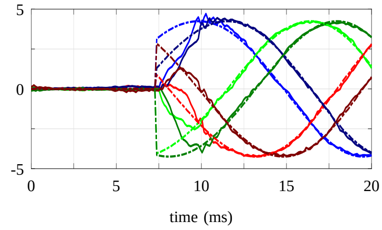

(c) Six-phase currents (A).

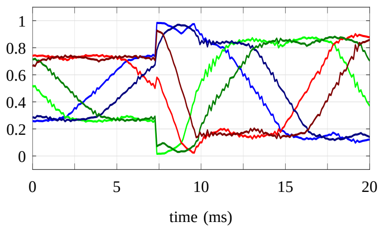

(d) Six-phase used average voltage (p.u.).

Fig. 21: Transient behavior of CCS-MPC at a torque reference step up.

[3] R. Bojoi, A. Tenconi, G. Griva, and F. Profumo, "Vector control of dual-three-phase induction-motor drives using two current sensors," *IEEE Trans. Ind. Appl.*, vol. 42, no. 5, pp. 1284–1292, Sep./Oct. 2006.

[4] G. Singh, K. Nam, and S. Lim, "A simple indirect field-oriented control scheme for multiphase induction machine," *IEEE Trans. Ind. Electron.*, vol. 52, no. 4, pp. 1177–1184, Aug. 2005.

[5] E. Levi, "Multiphase electric machines for variable-speed applications," *IEEE Trans. Ind. Electron.*, vol. 55, no. 5, pp. 1893–1909, May 2008.

[6] R. Bojoi, S. Rubino, A. Tenconi, and S. Vaschetto, "Multiphase electrical machines and drives: A viable solution for energy generation and transportation electrification," in *Proc. Eur. Power Electron. Conf.*, Iasi, Romania, 2016, pp. 632–639.

[7] M. J. Duran and F. Barrero, "Recent advances in the design, modeling, and control of multiphase machines—part ii," *IEEE Trans. Ind. Electron.*, vol. 63, no. 1, pp. 459–468, Jan. 2016.

[8] M. J. Duran, E. Levi, and F. Barrero, "Multiphase electric drives: Introduction," *Wiley encyclopedia of electrical and electronics engineering*, pp. 1–26, 1999.

[9] Y. Hu, Z. Q. Zhu, and M. Odavic, "Comparison of two-individual current control and vector space decomposition control for dual three-phase pmsm," *IEEE Trans. Ind. Appl.*, vol. 53, no. 5, pp. 4483–4492, Sep./Oct. 2017.

[10] P. Cortes, M. P. Kazmierkowski, R. M. Kennel, D. E. Quevedo, and J. Rodriguez, "Predictive control in power electronics and drives," *IEEE Trans. Ind. Electron.*, vol. 55, no. 12, pp. 4312–4324, Dec. 2008.

[11] J. Rodriguez, R. M. Kennel, J. R. Espinoza, M. Trincado, C. A. Silva, and C. A. Rojas, "High-performance control strategies for electrical drives: An experimental assessment," *IEEE Transactions on Industrial Electronics*, vol. 59, no. 2, pp. 812–820, Feb. 2012.

[12] S. Vazquez, J. Rodriguez, M. Rivera, L. G. Franquelo, and M. Norambuena, "Model predictive control for power converters and drives: Advances and trends," *IEEE Trans. Ind. Electron.*, vol. 64, no. 2, pp. 935–947, Feb. 2017.

[13] P. Karamanakos and T. Geyer, "Guidelines for the design of finite control set model predictive controllers," *IEEE Trans. Power Electron.*, vol. 35, no. 7, pp. 7434–7450, Jul. 2020.

[14] R. Bojoi, F. Farina, A. Tenconi, F. Profumi, and E. Levi, "Dual three-phase induction motor drive with digital current control in the stationary reference frame," *Power Engineer*, vol. 20, no. 3, pp. 40–43, Jun./Jul. 2006.

[15] I. Gonzalez-Prieto, M. J. Duran, J. J. Aciego, C. Martin, and F. Barrero, "Model predictive control of six-phase induction motor drives using virtual voltage vectors," *IEEE Trans. Ind. Electron.*, vol. 65, no. 1, pp. 27–37, Jan. 2018.

[16] P. F. Gonçalves, S. M. Cruz, and A. M. S. Mendes, "Disturbance observer based predictive current control of six-phase permanent magnet synchronous machines for the mitigation of steady-state errors and current harmonics," *IEEE Transactions on Industrial Electronics*, vol. 69, no. 1, pp. 130–140, Jan. 2022.

[17] Y. Zhao and T. Lipo, "Space vector pwm control of dual three-phase induction machine using vector space decomposition," *IEEE Trans. Ind. Appl.*, vol. 31, no. 5, pp. 1100–1109, Sep./Oct. 1995.

[18] B. Stumberger, G. Stumberger, D. Dolinar, A. Hamler, and M. Trlep, "Evaluation of saturation and cross-magnetization effects in interior

permanent-magnet synchronous motor," *IEEE Transactions on Industry Applications*, vol. 39, no. 5, pp. 1264–1271, 2003.

[19] S. Wendel, P. Karamanakos, P. Gebhardt, A. Dietz, and R. Kennel, "Flux linkage-based direct model predictive current control for synchronous machines," *IEEE Transactions on Power Electronics*, vol. 36, no. 12, pp. 14 237–14 256, 2021.

[20] J. Prieto, F. Barrero, C. S. Lim, and E. Levi, "Predictive current control with modulation in asymmetrical six-phase motor drives," in *2012 15th International Power Electronics and Motion Control Conference (EPE/PEMC)*, Gliwice, Poland, 2012, pp. LS1c.1–1–LS1c.1–8.

[21] Y.-R. Kim, S.-K. Sul, and M.-H. Park, "Speed sensorless vector control of induction motor using extended kalman filter," *IEEE Trans. Ind. Appl.*, vol. 30, no. 5, pp. 1225–1233, Sep./Oct. 1994.

[22] A. Favato, P. G. Carlet, F. Toso, R. Torchio, and S. Bolognani, "Integral model predictive current control for synchronous motor drives," *IEEE Trans. Power Electron.*, vol. 36, no. 11, pp. 13 293–13 303, Nov. 2021.

[23] D. Hadiouche, L. Baghli, and A. Rezzoug, "Space-vector pwm techniques for dual three-phase ac machine: analysis, performance evaluation, and dsp implementation," *IEEE Transactions on Industry Applications*, vol. 42, no. 4, pp. 1112–1122, Jul./Aug. 2006.

[24] Y. Hu, Z.-Q. Zhu, and K. Liu, "Current control for dual three-phase permanent magnet synchronous motors accounting for current unbalance and harmonics," *IEEE J. Emerg. Sel. Topics Power Electron.*, vol. 2, no. 2, pp. 272–284, Jun. 2014.

[25] Y. Hu, Z. Q. Zhu, and M. Odavic, "Torque capability enhancement of dual three-phase pmsm drive with fifth and seventh current harmonics injection," *IEEE Trans. Ind. Appl.*, vol. 53, no. 5, pp. 4526–4535, Sep./Oct. 2017.

[26] J. Xu, M. Odavic, Z.-Q. Zhu, Z.-Y. Wu, and N. M. A. Freire, "Modulation restraint analysis of space vector pwm for dual three-phase machines under vector space decomposition," *IEEE Transactions on Power Electronics*, vol. 36, no. 12, pp. 14 491–14 507, Dec. 2021.

[27] Q. Yang, P. Karamanakos, W. Tian, X. Gao, X. Li, T. Geyer, and R. Kennel, "Computationally efficient fixed switching frequency direct model predictive control," *IEEE Trans. Power Electron.*, vol. 37, no. 3, pp. 2761–2777, Mar. 2022.

Yitong Wu was born in Jilin, China, in 1997. He received the B.Eng. degree in automation from Tianjin University, Tianjin, China, in 2020. Since 2020, he has been a postgraduate and now a Ph. D candidate at the School of Electrical and Information engineering, Tianjin University. His research interests include electric drives, model predictive control, and embedded development.

Zhen Zhang (Senior Member, IEEE) received the B.Eng. and M.Eng. degrees in automation from Tianjin University, Tianjin, China, in 2004 and 2007, respectively, and the Ph.D. degree in electrical engineering from The University of Hong Kong, Hong Kong, in 2014.

Currently, he is a full Professor of electrical engineering with the School of Electrical and Information Engineering, Tianjin University. He has authored and coauthored more than 60 internationally refereed papers as well as two books published by Wiley-IEEE Press and Cambridge University Press, respectively. His research interests include advanced control for power conversion with emphasis on wireless power transfer and motor drives.

Dr. Zhang is currently the Chair of IEEE Beijing Section IES Chapter and an Associate Editor for the IEEE Transactions on Industrial Electronics, IEEE Transactions on Industrial Informatics, and IEEE Industrial Electronics Magazine. He is the recipient of the Humboldt Research Fellowship, Carl Friedrich von Siemens Research Fellowship, Japan Society for the Promotion of Science Visiting Fellowship, 2020 Best Paper Award for IEEE Transactions on Industrial Electronics, and IEEE Journal David Irwin Early Career Award.

Qifan Yang was born in Anhui, China, in 1995. He received the B.Eng. degree in electrical engineering Xi'an Jiaotong University, Xi'an, Shannxi, China, in 2016, and the M.Sc. degree in electrical power engineering from Technical University of Munich, Munich, Germany, in 2019. Since 2019, he has been pursuing the Ph.D. degree at the Chair of Electrical Drive Systems and Power Electronics, Technical University of Munich (TUM), Germany. His research interests include optimal control, power electronics and electrical drives.

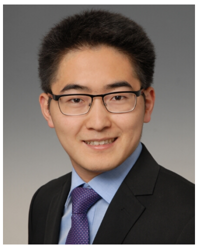

Wei Tian was born in Taizhou, Jiangsu, China, in 1989. He received the B.Eng. degree in electrical engineering and automation from Central South University (CSU), Changsha, China, in 2012 and the M.Sc. degree in electrical power engineering from RWTH Aachen University, Aachen, Germany, in 2015.

Since 2016, he has been pursuing the Ph.D. degree at the Chair of Electrical Drive Systems and Power Electronics, and the Chair of High-Power Converter Systems, Technical University of Munich (TUM), Munich, Germany. His research interests include power electronics and electrical drives, model predictive control, and modular multilevel converter.

Petros Karamanakos (S'10 – M'14 – SM'19) received the Diploma and Ph.D. degrees in electrical and computer engineering from the National Technical University of Athens (NTUA), Athens, Greece, in 2007, and 2013, respectively.

From 2010 to 2011 he was with the ABB Corporate Research Center, Baden-Dättwil, Switzerland, where he worked on model predictive control strategies for medium-voltage drives. From 2013 to 2016 he was a PostDoc Research Associate in the Chair of Electrical Drive Systems and Power Electronics, Technische Universität München, Munich, Germany. Since 2016, he has been with the Faculty of Information Technology and Communication Sciences, Tampere University, Tampere, Finland, where he is currently an Associate Professor. His main research interests lie at the intersection of optimal control, mathematical programming and power electronics, including model predictive control and optimal modulation for power electronic converters and ac variable speed drives.

Dr. Karamanakos received the 2014 Third Best Paper Award of the IEEE Transactions on Industry Applications and two Prize Paper Awards at conferences. He serves as an Associate Editor of the IEEE Transactions on Industry Applications and of the IEEE Open Journal of Industry Applications. He is a Regional Distinguished Lecturer of the IEEE Power Electronics Society in the years 2022 and 2023.

Marcelo Lobo Heldwein (S'99-M'08-SM'13) received the B.S. and M.S. degrees in electrical engineering from the Federal University of Santa Catarina (UFSC), Florian—polis, Brazil, in 1997 and 1999, respectively, and his Ph.D. degree from the Swiss Federal Institute of Technology (ETH Zurich), Zurich, Switzerland, in 2007.

He is currently the head of the Chair of High-Power Converter Systems with the Department of Energy and Process Engineering at the Technical University of Munich (TUM), Munich, Germany. From 1999 to 2003, he worked with industry, including R&D activities at the Power Electronics Institute, Brazil and Emerson Network Power, in Brazil and Sweden. He was a Postdoctoral Fellow at the ETH Zurich and at the UFSC from 2007 to 2009. From 2010 to 2022 he was a Professor with the Department of Electronics and Electrical Engineering at the UFSC. Dr. Heldwein is a member of the Brazilian Power Electronic Society (SOBRAEP) and a member of the Advisory Board of PCIM Europe. He is currently the Editor-in-Chief of the Brazilian Power Electronics Journal.

His research interests include Power Electronics, Advanced Power Distribution Technologies and Electromagnetic Compatibility.

Ralph Kennel (M'88-SM'96) was born in Kaiserslautern, Germany, in 1955. He received the Diploma and Dr. Ing. (Ph.D.) degrees in electrical engineering from University of Kaiserslautern, Kaiserslautern, Germany, in 1979 and 1984, respectively.

From 1983 to 1999, he worked on several positions with Robert BOSCH GmbH, Gerlingen, Germany. Until 1997, he was responsible for the development of servo drives. From 1994 to 1999, he was a Visiting Professor with the University of Newcastle-upon-Tyne, Newcastle-upon-Tyne, U.K. From 1999 to 2008, he was a Professor of electrical machines and drives with Wuppertal University, Wuppertal, Germany. Since 2008, he has been the head of the Chair of electrical drive systems and power electronics at Technical University of Munich, Munich, Germany. His current main interests include renewable energy systems, sensorless control of ac drives, predictive control of power electronics, and hardware-in-the-loop systems.

Dr. Kennel is a Chartered Engineer in the U.K., within IEEE, he is a Treasurer of the Germany Section as well as ECCE Global Partnership Chair of the Power Electronics society. He is currently an Associate Editor for the IEEE Transactions on Power Electronics.